Journal of Photonics for Energy

PhotonicsforEnergy.SPIEDigitalLibrary.org

Modeling approach to derive the anisotropic complex refractive index of polymer:fullerene blends for organic solar cells utilizing spectroscopic ellipsometry

Michael F. G. Klein
Gustavo Q. Glasner de Medeiros
Panagiota Kapetana
Uli Lemmer
Alexander Colsmann

SPIE.

Modeling approach to derive the anisotropic complex refractive index of polymer:fullerene blends for organic solar cells utilizing spectroscopic ellipsometry

Michael F. G. Klein, Gustavo Q. Glasner de Medeiros, Panagiota Kapetana, Uli Lemmer, and Alexander Colsmann*

Karlsruhe Institute of Technology (KIT), Light Technology Institute (LTI), Engesserstrasse 13, Karlsruhe, 76131, Germany

Abstract. The knowledge of the complex refractive indices of all thin layers in organic solar cells (OSCs) is a prerequisite for comprehensive optical device simulations that are particularly important for sophisticated device architectures, such as tandem OSCs. Therefore, refractive indices are often determined via spectroscopic ellipsometry and subsequent time-consuming modeling. Here, we investigate a modeling approach that allows for the determination of complex refractive indices of bulk-heterojunctions by superimposing the optical models of the respective fullerenes and polymers. The optical constants of neat [6,6]-phenyl C_{71}-butyric acid methyl ester ($PC_{71}BM$), poly{[4,4'-bis(2-ethylhexyl)dithieno(3,2-b;2',3'-d)silole]-2,6-diyl-*alt*-(2,1,3-benzothidiazole)-4,7-diyl} (PSBTBT) and poly[2,6-(4,4-bis(2-ethylhexyl)-4H-cyclopenta[2,1-b;3,4-b′′]dithiophene)-*alt*-4,7-(2,1,3-benzothiadiazole) (PCPDTBT) are determined, covering the OSC relevant spectral region from 250 to 1,000 nm. Then the blends PSBTBT:$PC_{71}BM$ and PCPDTBT:$PC_{71}BM$ are described within an effective medium approximation. From this approximation, the mass density ratio of polymer and fullerene can be derived. This approach furthermore allows for a uniaxial anisotropic optical description of the polymers and provides insight into thin-film morphology. In contrast to x-ray diffraction experiments, this method also allows for probing amorphous materials. Spectroscopic ellipsometry can be a valuable tool for the investigation of bulk-heterojunction morphologies of the latest high-performance OSC materials that exhibit a low degree of crystallinity. [DOI: 10.1117/1.JPE.5.057204]

Keywords: spectroscopic ellipsometry; organic solar cells; morphology; optical anisotropy; material densities.

Paper 14054SS received Aug. 18, 2014; accepted for publication Nov. 10, 2014; published online Jan. 6, 2015.

1 Introduction

Organic solar cells (OSCs) combine the advantages of low-cost and large-area fabrication with the use of nonhazardous and environmentally friendly materials. Over the last few years, power conversion efficiencies improved continuously, now exceeding 10% in single-junction solar cells.[1] Improvements often originated from the synthesis of new absorber materials that allowed for an enhanced spectral coverage of the solar spectrum or enabled higher internal quantum efficiencies.[2–7] In the lab, screening and optimization of new materials and cell architectures often follow a trial and error approach, although only very little amounts of material are available. An alternative and material saving route to optimized OSCs is a comprehensive optoelectronic device simulation that reduces the experimental parameter space. This becomes particularly important for sophisticated device architectures, such as tandem solar cells.[8] However, in order to carry out meaningful optical simulations, a profound knowledge of the refractive indices is mandatory.[5,9–12]

*Address all correspondence to: Alexander Colsmann, E-mail: alexander.colsmann@kit.edu

Unfortunately, optical constants from the literature often cannot be used to describe certain experiments since the optical properties strongly depend on the substrate, the underlying interface, the intrinsic polymer properties (molecular weight, polydispersity), the polymer:fullerene ratio, and the process conditions, such as the solvent system, the drying kinetics, and the postprocessing treatments.[13–24] Therefore, an urgent need for flexible optical descriptions of bulk-heterojunctions emerged, which use parametric descriptions and allow for individual adjustments.

If carried out purposefully, the optical model further reveals information about anisotropy within the bulk-heterojunction.[25] Such models were recently utilized to determine the vertical gradient in the active layer of OSCs[13,25] and to investigate the shape of [6,6]-phenyl C_{61}-butyric acid methyl ester ($PC_{61}BM$) inclusions in poly(3-hexylthiophene-2,5-diyl) (P3HT) solar cells.[26]

In this work, we present a modeling approach for spectroscopic ellipsometry (SE) data analysis, which facilitates the determination of the complex refractive indices of various polymer:fullerene blends. Therefore, in a first step, the relative dielectric functions of the fullerene [6,6]-phenyl C_{71}-butyric acid methyl ester ($PC_{71}BM$) and the polymers poly{[4,4'-bis(2-ethylhexyl)dithieno(3,2-b;2',3'-d)silole]-2,6-diyl-*alt*-(2,1,3-benzothidiazole)-4,7-diyl} (PSBTBT) and poly[2,6-(4,4-bis(2-ethylhexyl)-4H-cyclopenta[2,1-b;3,4-b'']dithiophene)-*alt*-4,7-(2,1,3-benzothiadiazole)] (PCPDTBT) are described by the superposition of Gaussian oscillators. In a second step, the relative dielectric functions of the polymer:fullerene blends are determined by superimposing the optical models of both constituents. PSBTBT and PCPDTBT are well-known donor-acceptor copolymers with good power conversion efficiencies when blended with $PC_{71}BM$.[27–31] Their similar structures allow a direct comparison. For the active layer deposition and blend ratios, we follow literature-known process protocols, which are optimized for high-performance solar cells.[27–29] Optical data are presented in the spectral region from 250 to 1,000 nm.

We further compare isotropic and anisotropic optical models of neat polymers. The results of this comparison serve as input parameters for anisotropic optical descriptions of the blends, which are then analyzed with respect to the predominant polymer orientation and the degree of aggregation.

2 Spectroscopic Ellipsometry

SE is a contactless and nondestructive measurement technique that allows for deriving the complex refractive indices of thin-films and their thicknesses simultaneously. The complex refractive index $\tilde{n}$, given by

$$\tilde{n} = n - ik = \sqrt{\tilde{\varepsilon}_r} = \sqrt{\varepsilon_{r,1} - i\varepsilon_{r,2}} \tag{1}$$

comprises the refractive index n (real part) and the extinction coefficient k (imaginary part) and is directly related to the complex relative dielectric function $\tilde{\varepsilon}_r$, assuming a relative permeability $\tilde{\mu}_r = 1$.

The basic ellipsometry working principle relies on measuring the change of the light beam polarization state after interacting with the sample. This change is described by the two ellipsometric values Ψ and Δ, which represent the amplitude ratio and phase difference between p- and s-polarization.[32] In this study, various wavelengths and angles of incidence were investigated. In addition, transmission spectra were recorded at normal incidence on the very same spot and incorporated into the analysis.

We use vendor-supplied software (WVASE32®, J. A. Woollam) to analyze the datasets. First, a multilayer model is constructed, where each individual layer describes a certain subset of physical properties of the sample, e.g., the level of interface intermixing, surface roughness, and the relative dielectric function of the material. In the following, "layer" will refer to a layer in the optical model and not necessarily to a physical layer.

The relative dielectric functions are defined by oscillator models, i.e., the description of each optical transition by an appropriate oscillator. Then the relative dielectric function $\tilde{\varepsilon}_r$ of a material can be described by the sum of these oscillators. To describe the transitions within the measurement range, we choose an oscillator type generating a Gaussian line shape in $\varepsilon_{r,2}$, Eq. (2), with a Kramers-Kronig consistent counterpart in $\varepsilon_{r,1}$, Eq. (3).

$$\varepsilon_{\mathrm{r},2,n}(E) = A_n e^{-\left[\frac{2\sqrt{\ln(2)}(E-E_n)}{Br_n}\right]^2} - A_{\mathrm{n}} e^{-\left[\frac{2\sqrt{\ln(2)}(E+E_{\mathrm{n}})}{Br_{\mathrm{n}}}\right]^2}, \tag{2}$$

$$\varepsilon_{\mathrm{r},1,n}(E) = \frac{2}{\pi} P \int_0^{\infty} \xi \frac{\varepsilon_{2,n}(\xi)}{\xi^2 - E^2} \mathrm{d}\xi, \tag{3}$$

where A_n is the amplitude, E_n is the center energy, Br_n is the width, and P is the principal value.[33] Higher-energy transitions outside the measurement range are summarized in a high-energy pole function, i.e., an oscillator with zero-width. Further, a real constant $\varepsilon_{\mathrm{r},\infty}$ is added to $\varepsilon_{\mathrm{r},1}$.

Based on this parameterized model, the optical response of the sample is calculated and compared to the measured Ψ and Δ data and the transmission. The parameters for the individual layers (thickness, oscillator parameters, etc.) are fitted in order to achieve a good match between model-generated and measured values. The difference between these values is quantified by the mean squared error (MSE).[34] MSE is used by the analysis software as weighted test function during the fitting procedure to further reduce the deviation between the three values by making use of the Marquardt-Levenberg algorithm.[35,36]

We verify the results of the fit and ensure physical significance of the calculated optical constants by, first, measuring the thicknesses of thin-films deposited on glass substrates in a transparent energy band by applying the Cauchy dispersion relation and by comparing them to profilometry results. (We note that the Cauchy model does not fulfill the Kramers-Kronig relation but is a valid approximation for transparent spectral regions.) Second, we perform a multisample analysis: several samples with varying thin-film thicknesses are characterized. All respective datasets are described with the same optical model, hence enabling a general and robust optical description and reducing parameter correlation.[37,38] In the end, the oscillator model will guarantee full Kramers-Kronig consistency.

Further, we include a wide range of angles of incidence in the analysis, typically ± 25 deg around the Brewster angle (step width: 5 deg). To perform the multisample analysis, the datasets are measured on several samples with different layer thicknesses. All SE investigations cover the spectral region from 250 to 1,700 nm (1,000 nm for $PC_{71}BM$) and layer thicknesses are determined in the transparent ($k = 0$) wavelength regime from 1,000 to 1,700 nm.

For reasons of clarity, we will show a reduced dataset in the following figures. In particular, we skip data in the infrared region beyond 1,000 nm, restrict to some representative angles of incidence, and only show typical data for one sample of the multisample analysis.

3 Experimental

3.1 *Spectroscopic Ellipsometry*

Ψ and Δ were measured with a variable angle spectroscopic ellipsometer (VASE®, J.A. Woollam Co., Inc.), equipped with a rotating analyzer and two detectors. A rotating retarder plate (MgF_2 Berek waveplate) in the beam path behind the fixed polarizer allows for a precise determination of Δ.[39] Datasets were recorded between 250 and 1,700 nm (1,000 nm for $PC_{71}BM$). Transmission data of the samples were collected at normal incidence and by moving the VASE detector arm into the optical path behind the sample. Thus, the transmission spectra were determined on the very same spot as the ellipsometric data, allowing for their incorporation into the analysis. The datasets were analyzed with the software WVASE32® (J. A. Woollam, version 3.774).

3.2 *Transmission Spectroscopy*

Transmission spectra of diluted solutions and of solid films spin cast onto quartz-glass substrates were recorded with a spectrophotometer (Lambda 1050, Perkin Elmer), enabling a lower noise level than the measurements carried out with the ellipsometer.

3.3 *Materials and Sample Preparation*

Soda-lime glass substrates were cleaned with acetone and isopropyl alcohol and then dried in a nitrogen stream. All materials were used as received and were deposited under inert conditions in a nitrogen glovebox (O_2 and $H_2O < 1$ ppm).

$PC_{71}BM$ (Solenne, >99%) was dissolved in DCB (anhydrous, 99%, Sigma-Aldrich®) at a concentration of 60 mg/mL, stirred overnight at 80°C, and spin cast on substrates at room temperature with different spin coater settings to achieve thicknesses between 85 and 120 nm.

PSBTBT and PCPDTBT were both dissolved in DCB with a concentration of 13 mg/mL, stirred overnight at 70 or 90°C, respectively, and were deposited from hot solution on hot soda-lime glass substrates. Different spin coater settings allowed for tuning the layer thicknesses between 40 and 60 nm for PSBTBT or 15 and 30 nm for PCPDTBT.

The blends PSBTBT:$PC_{71}BM$ (1:2, layer thicknesses between 90 and 115 nm) and PCPDTBT:$PC_{71}BM$ (1:3.4, layer thicknesses between 90 and 130 nm) with a polymer concentration of 13 mg/mL in DCB were spin coated following the same conditions used for neat films. The blend ratios were chosen according to optimized process protocols.[27,29]

SE data of the neat polymer films and the blend films were recorded between 250 and 1,700 nm at different angles of incidence α between 30 and 80 deg in 5 deg steps. Datasets were analyzed over the entire spectral range. For reasons of clarity, we only show a reduced dataset in the figures, i.e., we skip data in the infrared beyond 1,000 nm, restrict to some representative angles of incidence, and only show data for one sample of the multisample analysis.

Thin-film thicknesses were cross-checked with a stylus profiler (DektakXT, Bruker AXS GmbH) and compared with ellipsometry results.

4 Results and Discussion

4.1 *Glass Substrate*

Soda-lime glass is used as substrate for all thin-films.[37] Therefore, we first set up an optical model for the glass substrate. As the substrate is ~1 mm thick, unwanted backside reflections are expected. They can either be suppressed by roughening the substrate's backside or be accounted for in the analysis software. Here we use the latter approach as this allows measuring the transmission spectra on the very same spot after the ellipsometry characterization.

The glass substrate is described with a Cauchy dispersion relation[40] with an Urbach-tail[41] and a surface roughness layer of ~1.3 nm.

The derived complex refractive indices (n, k) of the soda-lime glass substrates are depicted in Fig. 1 versus wavelength. In the following, we keep the parameters of the model constant and treat the surface roughness layer as an intermixed layer of the subsequently applied thin-film and the glass substrate.

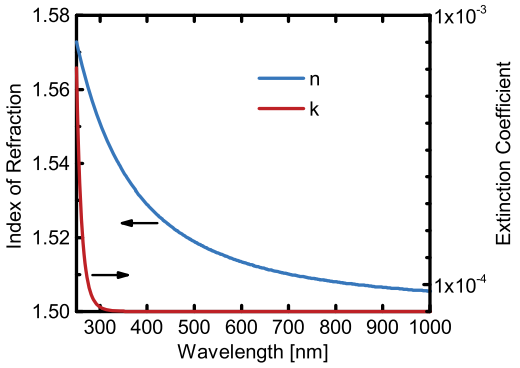

Fig. 1 Optical constants *n* and *k* of the soda-lime glass, which is used as substrate for all thin-films discussed in this study. The optical model includes a surface roughness layer of ~1.3 nm.

4.2 *$PC_{71}BM$*

Solar cells based on the polymers PCPDTBT and PSBTBT in combination with the electron acceptor $PC_{71}BM$ exhibit enhanced power conversion efficiencies. We first analyze $PC_{71}BM$. Therefore, the fullerene is dissolved in 1,2-dichlorobenzene (DCB) and then spin cast on the glass substrates as described in Sec. 3.3. A multisample SE analysis is performed on six samples with varying thicknesses. Figures 2(a) and 2(b) show the experimental data of a typical sample. Transmission spectra of $PC_{71}BM$ in DCB solution and of a solid $PC_{71}BM$ thin-film are recorded with a spectrophotometer, Fig. 2(c). From the absorption features present in all spectra, the starting values $E_{n,\mathrm{input}}$ for the center energies of the Gaussian oscillators are derived, Table 1. Based on this estimation of E_n, an optical model is set up comprising nine Gaussian oscillators Gau_n, a pole taking into account higher-energy transitions, and a real constant $\epsilon_{\mathrm{r},\infty}$. A stepwise fit (MSE = 11.14), starting from the infrared and progressing toward higher energies, results in the oscillator parameters given in Table 1. The fitted center energies E_n differ slightly from their respective starting values $E_{n,\mathrm{input}}$. In this multisample analysis, all measured datasets are taken into account. If the fit is restricted to a single sample, lower MSEs can be achieved. As the multisample analysis only differs slightly from the results of the single-sample analysis and as we aim, here and in the following, at finding a widely applicable optical model, we utilize the multisample approach. The model-generated data Ψ^{mod}, Δ^{mod}, and the optical constants are depicted in Figs. 2(a), 2(b), and 2(d), respectively. The good agreement with the optical constants in Ref. 42, supporting information, verifies the chosen approach. The good match between simulated and experimental transmission, which was measured on the same spot as the ellipsometry data, proves the fit quality, Fig. 3(a).

All thin-film thicknesses t_{Stylus} as determined by profilometry are well within the 90% confidence limit of the thickness t_{SE} as determined by SE.

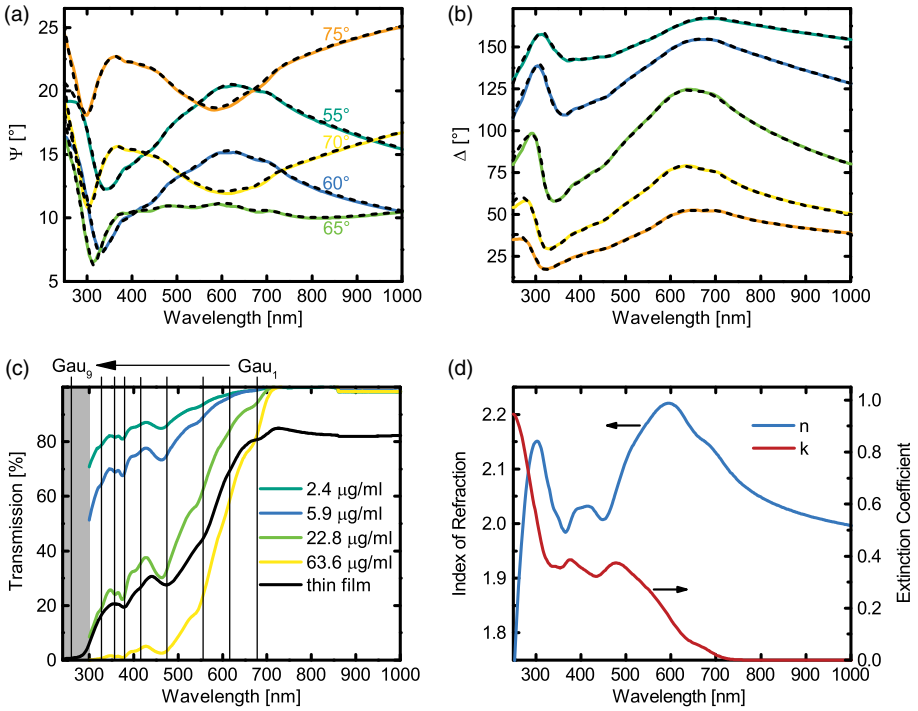

Fig. 2 (a) and (b) Spectroscopic ellipsometry data of an 87 nm [6,6]-phenyl C_{71}-butyric acid methyl ester ($PC_{71}BM$) thin-film spin cast on a glass substrate for five angles of incidence. The colored solid lines correspond to the measured data; the dashed black lines correspond to the model-generated data. (c) Transmission spectra of $PC_{71}BM$ in diluted dichlorobenzene (DCB) solutions and of a solid film on fused silica measured with a spectrophotometer. The gray shaded area indicates the absorption of the cuvettes. The center energies of the absorption features Gau_1 to Gau_9 are used as starting values for the Gaussian oscillator center energies in the optical model. (d) Optical constants n and k are derived from a multisample analysis.

Table 1 From the transmission spectra in Fig. 1(c), the starting values $E_{n,\mathrm{input}}$ for the fit of the Gaussian oscillators' center energies are derived. The optical model of [6,6]-phenyl C_{71}-butyric acid methyl ester ($PC_{71}BM$) comprises nine Gaussian oscillators (Gau_n with center energy E_n, amplitude A_n, and width Br_n,[33] a pole, and the real constant $\varepsilon_{r,\infty} = 2.00$ eV.

Oscillator	$E_{n,\mathrm{input}}$ (eV)	E_n (eV)	A_n (1)	Br_n (eV)
Gau_1	1.83	1.85	0.10	0.16
Gau_2	2.01	2.10	0.36	0.35
Gau_3	2.23	2.26	0.46	0.38
Gau_4	2.62	2.59	1.44	0.55
Gau_5	2.98	3.02	0.81	0.36
Gau_6	3.28	3.30	0.92	0.35
Gau_7	3.48	3.59	0.41	0.30
Gau_8	3.78	3.80	0.05	0.12
Gau_9	4.77	4.71	3.42	1.63
Pole	n/a	7.00	23.27	n/a

4.3 *Polymers*

Both polymers, PCPDTBT and PSBTBT, exhibit strong structural similarities. They differ only in the 5-position, where PCPDTBT comprises a carbon atom, whereas PSBTBT features a silicon atom, Fig. 4(a). It was shown that the silicon substitution in PSBTBT reduces the steric hindrance from the bulky alkyl groups and improves molecular packing.[43] The main absorption features of both polymers are still comparable though.

The measured datasets Ψ and Δ for a PSBTBT thin-film spin cast on a glass substrate are shown in Figs. 5(a) and 5(b), respectively. The isotropic optical model is constructed in analogy to the procedure described for $PC_{71}BM$. The transmission spectra of PSBTBT in DCB solution and of a solid PSBTBT thin-film are recorded, Fig. 5(c). The analysis of the absorption features leads to the starting values $E_{n,\mathrm{input}}$ for the center energies E_n of the Gaussian oscillators. Then, all oscillator parameters, a pole for the high-energy transitions and $\varepsilon_{r,\infty}$ are fitted. The respective values are summarized in Table 2. Based on this model, the isotropic optical constants are derived, Fig. 6(a).

PCPDTBT is investigated accordingly. The respective isotropic datasets are shown in Fig. 7, Table 3, and Fig. 6(b). The spectral shape of the complex indices of refraction is comparable with the isotropic data presented by Guerrero et al.[42] As they used PCPDTBT from a different supplier, the amplitudes are different though.

Both polymer models are derived independently. However, the derived optical models utilize very similar sets of Gaussian oscillators, which reflect their strong structural similarity. A comparison of the isotropic optical constants further shows that the overall optical density of PSBTBT is somewhat higher than the optical density of PCPDTBT. This can be either attributed to a higher intrinsic absorption or to a denser packing of the polymer chains.[43]

For both polymers, we assign the transitions Gau_1 and Gau_2 to the 0–0 and 0–1 absorption peaks, while Gau_3 comprises higher vibronic progressions and an amorphous background. The nature of Gau_4 remains unclear, but may be attributed to transitions involving more localized states.[44]

A more detailed model has to take into account the anisotropy of the films. OSC polymers often exhibit elongated structures and, hence, form mostly flat two-dimensional molecules.[45–48] Therefore, we probe the thin-films for anisotropy, assuming no preferential order in the in-plane direction as indicated by the invariance of Ψ under in-plane sample rotation.[32,49,50] This assumption allows us to utilize a uniaxial optical description, only distinguishing between

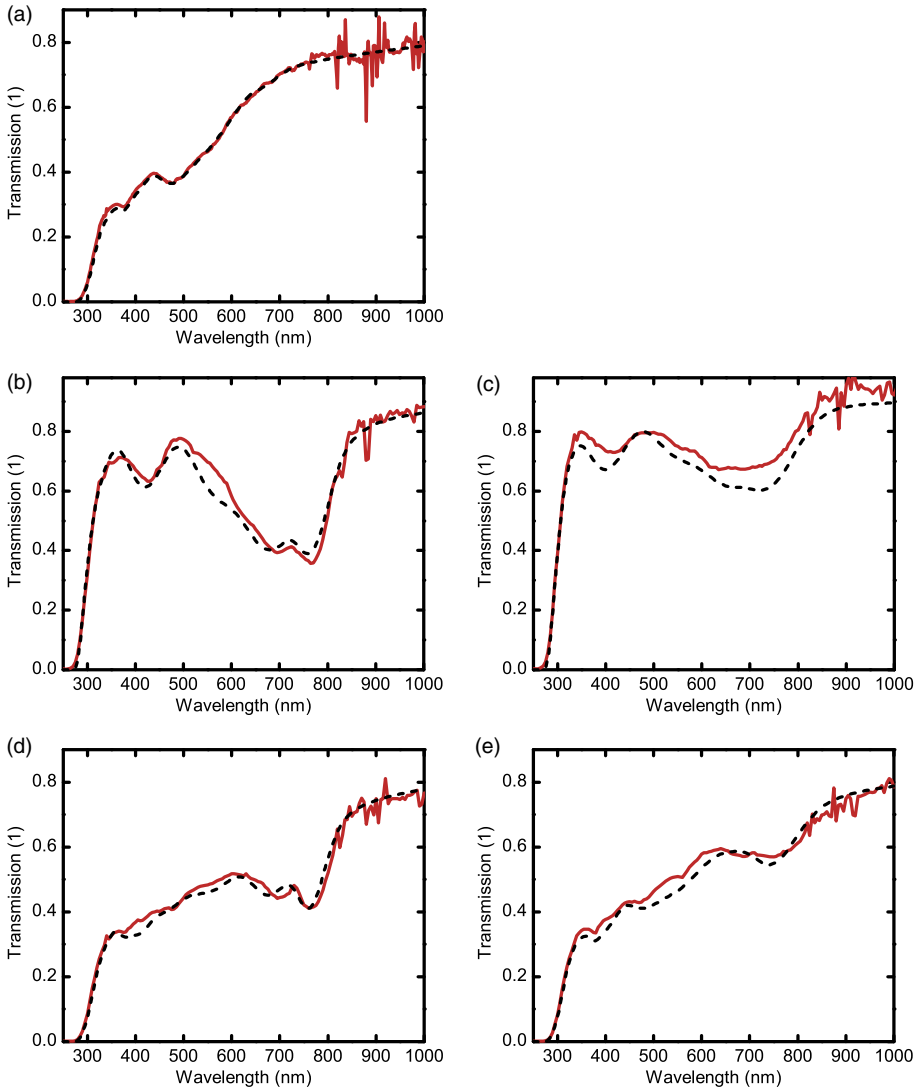

Fig. 3 Measured (red lines) and simulated transmission (black dashed lines) of (a) $PC_{71}BM$, (b) poly{[4,4'-bis(2-ethylhexyl)dithieno(3,2-b;2',3'-d)silole]-2,6-diyl-*alt*-(2,1,3-benzothidiazole)-4,7-diyl} (PSBTBT), (c) poly[2,6-(4,4-bis(2-ethylhexyl)-4H-cyclopenta[2,1-b;3,4-b′′]dithiophene)-*alt*-4,7-(2,1,3-benzothiadiazole)] (PCPDTBT), (d) PSBTBT:$PC_{71}BM$, and (e) PCPDTBT:$PC_{71}BM$. The measured transmission spectra were determined at the same spot as the ellipsometry data by rotating the ellipsometer's detector straight behind the sample. The noise levels are higher than in the spectrophotometer measurements that were described in Sec. 3.2 and that are depicted in Figs. 2(c), 5(c), and 7(c). The simulated data in Figs. 3(b)–3(e) rely on anisotropic models.

the xy- and the z-contribution. [The xy-component is sometimes referred to as $\|$ (in-plane) and z as $\perp$ (out-of-plane).] For this orientation, the off-diagonal elements of the Jones matrix vanish.[32]

In the uniaxial configuration, the optical constants n_{xy} and k_{xy} are determined by the xy-layer, and the z-component by the z-layer. The xy-optical constants describe light-matter interaction for light under normal incidence with its electrical field vector E parallel to the sample surface. For light impinging at grazing incidence, E is almost normal to the sample surface and the interaction with the polymer is described with n_z and k_z.

For the anisotropic model, the isotropic oscillator parameters serve as input parameters for both the xy- and z-layer, consequently doubling the number of fit parameters. Since doubling of the fit parameters does hamper finding a unique solution, we simplify our model by assuming that the same optical transitions will be observed in both directions (xy and z), changing their relative amplitude only. Accordingly, the oscillator amplitudes $A_{n,xy}$ and $A_{n,z}$ are defined as fit parameters.

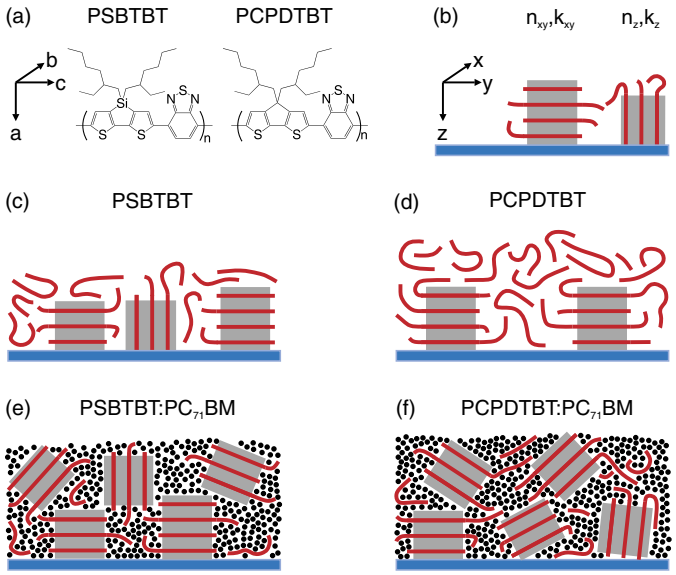

Fig. 4 (a) Chemical structure of PSBTBT and PCPDTBT and definition of the polymer-chain reference frame (a, b, and c). The *c* axis is oriented along the polymer backbone. (b) The optical constants n_{xy} and k_{xy} describe light-polymer interaction for polymers with their *c* axes being aligned parallel to the substrate surface, while the *z*-component describes vertically oriented polymers. (*x*, *y*, and *z*) is the substrate reference frame. Schemes of the morphology of (c) neat PSBTBT, (d) neat PCPDTBT, (e) PSBTBT : $PC_{71}BM$, and (f) PCPDTBT : $PC_{71}BM$ showing different degrees of aggregate alignment relative to the surface. Black dots represent $PC_{71}BM$.

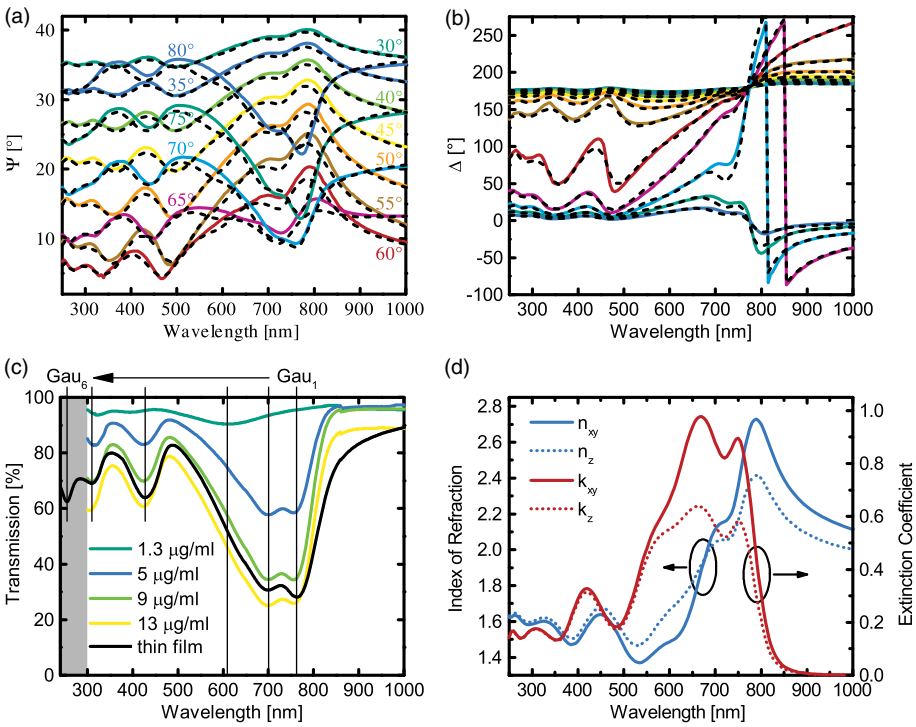

Fig. 5 (a) and (b) Spectroscopic ellipsometry data Ψ and Δ of a typical neat PSBTBT thin-film spin cast on a glass substrate. The colored solid lines correspond to the measured data; the dashed black lines correspond to data generated from a uniaxial optical model. (c) Transmission spectra of PSBTBT in diluted DCB solutions and of a solid film on fused silica. The starting values for the Gaussian oscillator center energies $E_{n,\mathrm{input}}$ are derived from the center energies of the absorption features, Table 2. (d) The optical constants comprise an in-plane (index *xy*) and out-of-plane component (index *z*) and are derived from a multisample analysis with an overall mean squared error $(\mathrm{MSE}) = 6.37$.

Table 2 Isotropic, parameterized description of poly{[4,4'-bis(2-ethylhexyl)dithieno(3,2-b;2',3'-d) silole]-2,6-diyl-*alt*-(2,1,3-benzothidiazole)-4,7-diyl} (PSBTBT). The starting values $E_{n,\mathrm{input}}$ are derived from the transmission spectra in Fig. 5(c). The center energies E_n change only slightly upon performing the fit. The parameters A_n and Br_n are determined defining the Gaussian oscillators Gau_n. The offset was found to be $\varepsilon_{r,\infty} = 2.46$ eV.

Oscillator	$E_{n,\mathrm{input}}$ (eV)	E_n (eV)	A_n (1)	Br_n (eV)
Gau_1	1.63	1.62	0.10	0.16
Gau_2	1.77	1.79	0.36	0.35
Gau_3	2.04	2.08	0.46	0.38
Gau_4	2.90	2.92	1.44	0.55
Gau_5	4.01	4.01	0.81	0.36
Gau_6	4.86	4.87	0.92	0.35
Pole	n/a	5.52	4.46	n/a

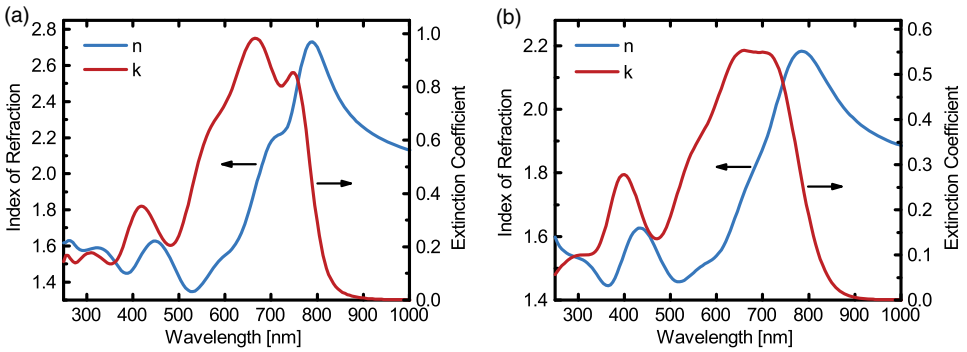

Fig. 6 Optical constants of (a) PSBTBT and (b) PCPDTBT within an isotropic description. We note the different scaling of the *y* axes.

The fitted datasets Ψ and Δ for PSBTBT are shown in Figs. 5(a) and 5(b) and the derived anisotropic optical constants in Fig. 5(d). The MSE improves from 7.23 to 6.37 upon utilizing an anisotropic model. The respective datasets for PCPDTBT are shown in Fig. 7. For PCPDTBT, the MSE improves from 7.77 to 7.51. Evidence of the fit quality is provided in Figs. 3(b) and 3(c), where we compare the experimental transmission data that were measured on the same spot as the ellipsometry data, with the simulated transmission based on the ellipsometric model. Both neat polymers exhibit pronounced uniaxial anisotropy. Since the polymer $\pi \rightarrow \pi^*$ transitions, here modeled with Gau_1—Gau_3, are excited by an electrical field that is polarized parallel to the polymer backbone, i.e., the polymer *c* axis as defined in Fig. 4(a), a detailed analysis of the anisotropic optical constants can further reveal morphological details.[51,52,53] The optical constants n_{xy} and k_{xy} describe light-polymer interaction for polymers with their *c* axes aligned parallel to the substrate surface, while the z-component describes upright polymers with their *c* axes oriented in *z*-direction, Fig. 4(b).

The extinction coefficient of PSBTBT splits up in an *xy*- and a *z*-component between ~540 and 800 nm, Fig. 5(d). Toward lower wavelengths, no splitting is observed, indicating a different nature of the involved transitions. According to similar observations in the literature, we attribute the shoulder around 761 nm (Gau_1) to polymer aggregation.[43] As the contribution of the *xy*-component is more pronounced than the contribution of the *z*-component, we conclude that aggregates of polymers with a *c* axis aligned in-plane prevail, Fig. 4(c).

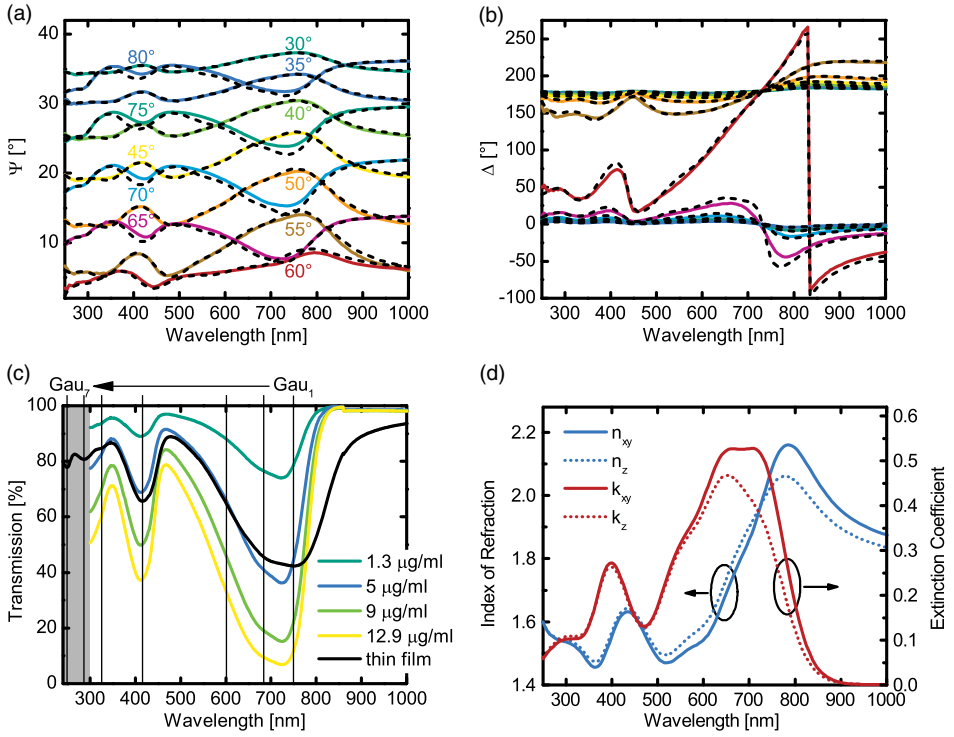

Fig. 7 (a) and (b) Spectroscopic ellipsometry data Ψ and Δ of a typical neat PCPDTBT thin-film spin cast on a glass substrate. The solid lines correspond to the measured data; the dashed black lines correspond to the model-generated data within a uniaxial description. (c) Transmission spectra of PCPDTBT in dilute DCB solutions and of a film on fused silica. The center energies $E_{n,\text{input}}$ of the absorption features Gau_n are given in Table 3. (d) Anisotropic optical constants derived from a multisample analysis with an overall MSE = 7.51.

For PCPDTBT, the *xy*- and *z*-extinction coefficients also split up and show anisotropic behavior in the low-wavelength regime, Fig. 7(d). The low-energy shoulder, which is visible in the k_{xy} data, does not appear in the k_z data. In analogy to PSBTBT, the shoulder in k_{xy} can be attributed to aggregates of polymers with *c* axes aligned parallel to the *xy*-plane, whereas the interpretation of k_z leads to ambiguous results. This can either be attributed to nonaggregated standing polymers or an isotropic amorphous background, Fig. 4(d).

Table 3 Poly[2,6-(4,4-bis(2-ethylhexyl)-4H-cyclopenta[2,1-b;3,4-b′′]dithiophene)-*alt*-4,7-(2,1,3-benzothiadiazole] (PCPDTBT). Starting values $E_{n,\text{input}}$ as derived from Fig. 4(c). The parameters E_n, A_n, and Br_n determine the optical model. $\varepsilon_{r,\infty} = 2.28$ eV. Gau_7 is outside the ellipsometer's measurement range; the pole function covers its contribution.

Oscillator	$E_{n,\text{input}}$ (eV)	E_n (eV)	A_n (1)	Br_n (eV)
Gau_1	1.66	1.66	1.21	0.21
Gau_2	1.81	1.84	1.42	0.34
Gau_3	2.06	2.17	1.00	0.57
Gau_4	2.98	3.06	0.72	0.62
Gau_5	3.80	3.89	0.16	1.75
Gau_6	4.34	4.34	0.15	2.20
Gau_7	4.98	n/a	n/a	n/a
Pole	n/a	5.83	5.28	n/a

4.4 *Blends*

The measured spectroscopic ellipsometry data Ψ and Δ of a PSBTBT:$PC_{71}BM$ and a PCPDTBT:$PC_{71}BM$ thin-film are depicted in Figs. 8(a) and 8(c) and in Figs. 8(b) and 8(d), respectively. The optical properties of the polymer:fullerene blends are modeled within an effective medium approximation (EMA). Therefore, the optical constants of polymer and fullerene constituents are superimposed. As the analysis of neat polymers in Sec. 4.3 revealed a preferred orientation of the PSBTBT and PCPDTBT *c* axes parallel to the substrate, we choose uniaxial models for the blends as well. The oscillator parameters in Tables 1, 2, and 3 are used as starting parameters.

After determining the layer thicknesses in the transparent spectral regime, the volume ratio of polymer to $PC_{71}BM$ is fitted. The resulting ratios are listed in Table 4 showing excellent agreement with volume ratios being calculated on the basis of material density as determined by helium pycnometry in the literature.[54,55] This result shows that SE can be an alternative and contactless metrology approach to determine material density ratios in blend films. If the

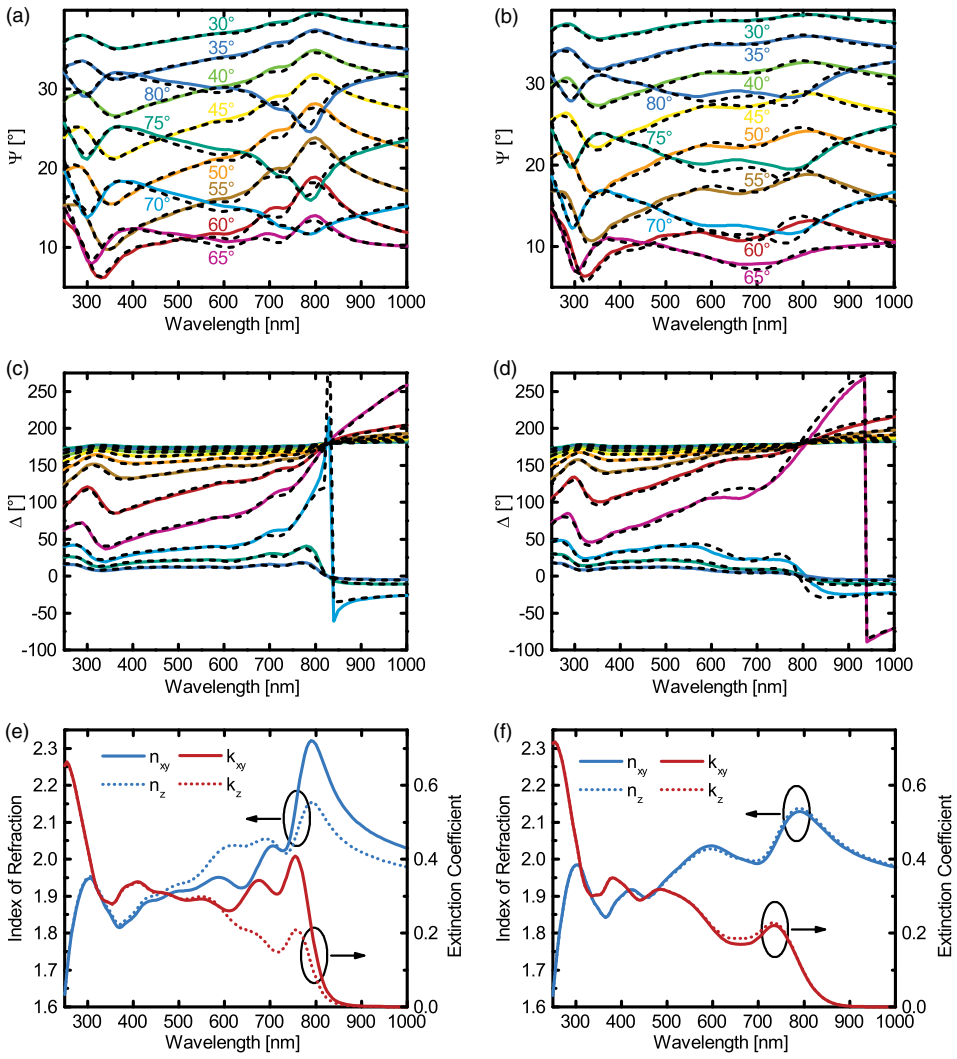

Fig. 8 Spectroscopic ellipsometry data Ψ and Δ of [(a) and (c)] a typical PSBTBT:$PC_{71}BM$ (1:2) thin-film and [(b) and (d)] a typical PCPDTBT:$PC_{71}BM$ (1:3.4) thin-film. The solid lines correspond to the measured data; the dashed black lines correspond to the model-generated data within a uniaxial description. Anisotropic optical constants of (e) PSBTBT:$PC_{71}BM$ and (f) PCPDTBT:$PC_{71}BM$ are derived from a multisample analysis with an overall MSE = 3.90 and MSE = 4.64, respectively.

Table 4 The normalized volume ratios in the blends as derived from ellipsometry fittings show excellent agreement with the volume ratio calculated from the material densities. $\rho_{PC71BM} = 1.52$ g/cm^3, $\rho_{PSBTBT} = 1.17$ g/cm^3, and $\rho_{PCPDTBT} = 1.10$ g/cm^3 as determined by helium pycnometry in the group of Dadmun et al.[54,55]

Quantity	Initial ratio	Normalized volume ratio	Normalized volume ratio
Method	By weight	Pycnometry[54,55]	Ellipsometry fit
PSBTBT:PC_{71}BM	1:2.0	39.4:60.6	39.2:60.8
PCPDTBT:PC_{71}BM	1:3.4	28.9:71.1	29.0:71.0

material density of one component is already known, the absolute material density of the other component can be determined.

In the next step, we investigate whether the polymer's anisotropy is preserved upon blending with $PC_{71}BM$. Therefore, the polymer oscillator amplitudes are fitted leading to the anisotropic optical constants shown in Fig. 8(e) for PSBTBT:PC_{71}BM and in Fig. 8(f) for PCPDTBT:PC_{71}BM. As indicated in Figs. 8(a) and 8(c) and in Figs. 8(b) and 8(d), both multi-sample fits describe the experimental data very well (MSE = 3.90 and 4.64). Again, the comparison of the simulated and the experimental transmission in Figs. 3(d) and 3(e) confirms the good fit quality. Further, the anisotropic optical constants of PSBTBT:PC_{71}BM match the shape of the isotropic optical constants known in the literature.[56] When performing the fits, only the amplitudes of the oscillators Gau_1 to Gau_3 change considerably. In analogy to the analysis of the neat polymers, those oscillators are an indicator for the degree of polymer aggregation.

For PSBTBT:PC_{71}BM, a pronounced uniaxial anisotropy becomes visible in the optical constants, Fig. 8(e). Similar to neat PSBTBT, both the in-plane and the out-of-plane extinction coefficients exhibit shoulders around 760 nm, where the *xy*-contribution dominates the *z*-contribution. The dominance of the *xy*-contribution can be attributed to polymer aggregates with their *c* axes aligned in-plane as illustrated in Fig. 4(e). This interpretation of the polymer orientation from SE experiments fits well to the time-resolved x-ray analysis that we published earlier, where we found that PSBTBT nucleation takes place in defined orientation at an interface, while randomly oriented aggregates form in the bulk during solvent evaporation.[29] As the degree of PSBTBT:PC_{71}BM anisotropy is similar to the anisotropy of neat PSBTBT, the polymer orientation remains mostly unaffected upon blending with $PC_{71}BM$.

For PCPDTBT:PC_{71}BM, the optical constants in *xy*- and in *z*-directions differ slightly, Fig. 8(f). The PCPDTBT low-energy shoulder appears in both directions. This can be attributed to randomly oriented PCPDTBT aggregates as depicted in Fig. 4(f). In the blend model, the low-energy shoulder is more pronounced than in the model for neat PCPDTBT, indicating a higher degree of aggregation in the blend.

The higher degree of the *c* axis in-plane alignment within the PSBTBT:PC_{71}BM blend as compared to the PCPDTBT:PC_{71}BM blend, probably induced by the substrate surface, may be explained by the lower $PC_{71}BM$ volume fraction, Table 4.

4.5 *Limitations*

The EMA approach requires negligible cross-coupling of optical transitions between the blend's components. For example, charge transfer (CT) absorption could cause such a new excitation channel. Since CT absorption in state-of-the-art OSCs is some magnitudes lower than the $\pi \rightarrow \pi^*$ transition,[57] we disregard CT absorption.

Both polymers that are investigated in this study exhibit a lower degree of crystallinity than other semicrystalline materials, such as P3HT.[58] Upon blending more crystalline materials, the degree of crystallinity may be reduced significantly. Therefore, in order to generate a suitable model for highly crystalline materials, care should be taken that the degree of crystallinity between the neat material and the blend is comparable. For example, for neat P3HT, we suggest deposition from a low-boiling point solvent, such as chloroform, thus accelerating the film drying time and, thereby, effectively suppressing crystallization of the neat polymer.

The determination of the anisotropic blend models benefits from the weak spectral overlap of the polymer and fullerene extinction coefficients, which allows separating both components and performing a precise fit. Fortunately, this applies to the vast majority of polymer:fullerene blends. Even more stable fit results can be achieved by taking into account advanced photophysical descriptions.[59] So far, such a detailed description has been elaborated for P3HT only.[60,61] A description of the complex absorption spectra of the low-band gap polymers is still lacking. Therefore, we suggest utilizing the phenomenological derived values of the oscillator center energies and robust multisample fits as discussed in this work.

5 Conclusion

In conclusion, we present a modeling approach for the analysis of ellipsometry data, which facilitates the precise determination of the optical constants of various polymer:fullerene blends. The optical constants of the neat constituents $PC_{71}BM$, PSBTBT, and PCPDTBT are determined, first, by parameterizing the constituents' relative dielectric functions, where each optical excitation is described by a Gaussian oscillator. The center energies of the oscillators are derived phenomenologically from their respective transmission spectra.

Based on this set of optical constants, the blends PSBTBT:$PC_{71}BM$ and PCPDTBT:$PC_{71}BM$ are described within an EMA. An initial fit on the polymer-to-fullerene ratio allows to derive the volume density ratio of both constituents.

Our approach further allows for considering a uniaxial anisotropic optical description of the neat polymers and their blends. The detailed analysis of the anisotropy provides deep insight into the PSBTBT, PCPDTBT, and blend morphology. Since many of the latest high-performance materials exhibit a lower degree of crystallinity than the vastly studied P3HT,[62] we propose SE as a nondestructive bulk-heterojunction probing technique for future polymer:fullerene bulk-heterojunction investigations.

Acknowledgments

The authors acknowledge funding by the Federal Ministry of Education and Research (BMBF) within the project Taurus, contract 03EK3504, the Deutsche Forschungsgemeinschaft (DFG) priority program 1355 "Elementary Processes of Organic Photovoltaics," and the State of Baden-Württemberg through the DFG Center for Functional Nanostructures (CFN). Poly [2,6-(4,4-bis(2-ethylhexyl)-4H-cyclopenta[2,1-b;3,4-b′′]dithiophene)-*alt*-4,7-(2,1,3-benzothiadiazole)] and poly{[4,4'-bis(2-ethylhexyl)dithieno(3,2-b;2',3'-d)silole]-2,6-diyl-*alt*-(2,1,3-benzothidiazole)-4,7-diyl} were supplied from Konarka. The authors thank Professor M. Dadmun, Professor G. Bazan, Dr. H. Chen, Dr. J. Peet, Dr. S. Hu, and Dr. J. Azoulay for the communication of their results[54,55] prior to publication, Dr. B. Schmidt-Hansberg (Karlsruhe Institute of Technology) for fruitful discussions, and Dr. T. Wagner (LOT-QuantumDesign) for technical support. M.F.G.K. was supported by the Karlsruhe School of Optics and Photonics (KSOP).

References

1. M. A. Green et al., "Solar cell efficiency tables (version 41)," *Prog. Photovoltaics Res. Appl.* **21**, 1–11 (2013).
2. H.-Y. Chen et al., "Polymer solar cells with enhanced open-circuit voltage and efficiency," *Nat. Photonics* **3**, 649–653 (2009).
3. S. H. Park et al., "Bulk heterojunction solar cells with internal quantum efficiency approaching 100%," *Nat. Photonics* **3**, 297–302 (2009).
4. Y. Liang et al., "For the bright future—bulk heterojunction polymer solar cells with power conversion efficiency of 7.4%," *Adv. Mater.* **22**, E135–E138 (2010).
5. H. Azimi et al., "Determining the internal quantum efficiency of organic bulk heterojunctions based on mono and bis-adduct fullerenes as acceptor," *Sol. Energy Mater. Sol. Cells* **95**, 3093–3098 (2011).

6. L. Dou et al., "Tandem polymer solar cells featuring a spectrally matched low-bandgap polymer," *Nat. Photonics* **6**, 180–185 (2012).
7. Y. Sun et al., "Solution-processed small-molecule solar cells with 6.7% efficiency," *Nat. Mater.* **11**, 44–48 (2012).
8. A. Puetz et al., "Solution processable, precursor based zinc oxide buffer layers for 4.5% efficient organic tandem solar cells," *Org. Electron.* **13**, 2696–2701 (2012).
9. G. Dennler et al., "Angle dependence of external and internal quantum efficiencies in bulk-heterojunction organic solar cells," *J. Appl. Phys.* **102**, 054516 (2007).
10. L. A. A. Pettersson, L. S. Roman, and O. Inganäs, "Modeling photocurrent action spectra of photovoltaic devices based on organic thin films," *J. Appl. Phys.* **86**, 487–496 (1999).
11. T. Ameri et al., "Fabrication, optical modeling, and color characterization of semitransparent bulk-heterojunction organic solar cells in an inverted structure," *Adv. Funct. Mater.* **20**, 1592–1598 (2010).
12. H. Hoppe et al., "Modeling of optical absorption in conjugated polymer/fullerene bulk-heterojunction plastic solar cells," *Thin Solid Films* **451–452**, 589–592 (2004).
13. M. Campoy-Quiles et al., "Morphology evolution via self-organization and lateral and vertical diffusion in polymer:fullerene solar cell blends," *Nat. Mater.* **7**, 158–164 (2008).
14. A. M. C. Ng et al., "Spectroscopic ellipsometry characterization of polymer-fullerene blend films," *Thin Solid Films* **517**, 1047–1052 (2008).
15. B. Schmidt-Hansberg et al., "In situ monitoring the drying kinetics of knife coated polymer-fullerene films for organic solar cells," *J. Appl. Phys.* **106**, 124501 (2009).
16. T. Wang et al., "The development of nanoscale morphology in polymer:fullerene photovoltaic blends during solvent casting," *Soft Matter* **6**, 4128–4134 (2010).
17. T. Agostinelli et al., "Real-time investigation of crystallization and phase-segregation dynamics in P3HT:PCBM solar cells during thermal annealing," *Adv. Funct. Mater.* **21**, 1701–1708 (2011).
18. M. Sanyal et al., "In situ x-ray study of drying-temperature influence on the structural evolution of bulk-heterojunction polymer-fullerene solar cells processed by doctor-blading," *Adv. Energy Mater.* **1**, 363–367 (2011).
19. M. F. G. Klein et al., "Oligomers comprising 2-phenyl-2H-benzotriazole building blocks for solution-processable organic photovoltaic devices," *J. Phys. Chem. C* **116**, 16358–16364 (2012).
20. M. F. G. Klein et al., "Poly(3-hexylselenophene) solar cells: correlating the optoelectronic device performance and nanomorphology imaged by low-energy scanning transmission electron microscopy," *J. Polym. Sci., Part B: Polym. Phys.* **50**, 198–206 (2012).
21. B. Schmidt-Hansberg et al., "Investigation of non-halogenated solvent mixtures for high throughput fabrication of polymer-fullerene solar cells," *Sol. Energy Mater. Sol. Cells* **96**, 195–201 (2012).
22. M. F. G. Klein et al., "Carbazole-phenylbenzotriazole copolymers as absorber material in organic solar cells," *Macromolecules* **46**, 3870–3878 (2013).
23. K. Sun et al., "The role of solvent vapor annealing in highly efficient air-processed small molecule solar cells," *J. Mater. Chem. A* **2**, 9048–9054 (2014).
24. D. M. DeLongchamp et al., "Molecular characterization of organic electronic films," *Adv. Mater.* **23**, 319–337 (2011).
25. P. Karagiannidis et al., "Evolution of vertical phase separation in P3HT:PCBM thin films induced by thermal annealing," *Mater. Chem. Phys.* **129**, 1207–1213 (2011).
26. S. Engmann et al., "Ellipsometric investigation of the shape of nanodomains in polymer/fullerene films," *Adv. Energy Mater.* **1**, 684–689 (2011).
27. J. K. Lee et al., "Processing additives for improved efficiency from bulk heterojunction solar cells," *J. Am. Chem. Soc.* **130**, 3619–3623 (2008).
28. R. C. Coffin et al., "Streamlined microwave-assisted preparation of narrow-bandgap conjugated polymers for high-performance bulk heterojunction solar cells," *Nat. Chem.* **1**, 657–661 (2009).
29. B. Schmidt-Hansberg et al., "Structure formation in low-bandgap polymer:fullerene solar cell blends in the course of solvent evaporation," *Macromolecules* **45**, 7948–7955 (2012).

30. J. Hou et al., "Synthesis, characterization, and photovoltaic properties of a low band gap polymer based on silole-containing polythiophenes and 2,1,3-benzothiadiazole," *J. Am. Chem. Soc.* **130**, 16144–16145 (2008).
31. P. Boland, K. Lee, and G. Namkoong, "Device optimization in PCPDTBT:PCBM plastic solar cells," *Sol. Energy Mater. Sol. Cells* **94**, 915–920 (2010).
32. H. Fujiwara, *Spectroscopic Ellipsometry: Principles and Applications*, John Wiley & Sons, Chichester, England, United Kingdom (2007).
33. K.-E. Peiponen and E. M. Vartiainen, "Kramers-Kronig relations in optical data inversion," *Phys. Rev. B: Condens. Matter Mater. Phys.* **44**, 8301–8303 (1991).
34. J. A. Woollam Company, *Guide to Using WVASE32—Spectroscopic Ellipsometry Data Acquisition and Analysis Software*, J. A. Woollam Co., Lincoln, NE (2008).
35. G. E. Jellison, Jr., "Use of the biased estimator in the interpretation of spectroscopic ellipsometry data," *Appl. Opt.* **30**, 3354–3360 (1991).
36. C. M. Herzinger et al., "Ellipsometric determination of optical constants for silicon and thermally grown silicon dioxide via a multi-sample, multi-wavelength, multi-angle investigation," *J. Appl. Phys.* **83**, 3323–3336 (1998).
37. A. Ng et al., "Accurate determination of the index of refraction of polymer blend films by spectroscopic ellipsometry," *J. Phys. Chem. C* **114**, 15094–15101 (2010).
38. A. Ng et al., "Annealing of P3HT:PCBM blend film—the effect on its optical properties," *ACS Appl. Mater. Interfaces* **5**, 4247–4259 (2013).
39. D. Aspnes and J. Law, "Ellipsometer and polarimeter with zero-order plate compensator," U.S. 6181421 (2001).
40. M. A. L. Cauchy, *Mémoire sur la dispersion de la lumière*, Calve, Prague (1836).
41. H. Tompkins and W. McGahan, *Spectroscopic Ellipsometry and Reflectometry: A User's Guide*, Wiley, New York (1999).
42. A. Guerrero et al., "Interplay between fullerene surface coverage and contact selectivity of cathode interfaces in organic solar cells," *ACS Nano* **7**, 4637–4646 (2013).
43. H.-Y. Chen et al., "Silicon atom substitution enhances interchain packing in a thiophene-based polymer system," *Adv. Mater.* **22**, 371–375 (2010).
44. T. Agostinelli et al., "The role of alkane dithiols in controlling polymer crystallization in small band gap polymer:fullerene solar cells," *J. Polym. Sci., Part B: Polym. Phys.* **49**, 717–724 (2011).
45. M. Sanyal et al., "Effect of photovoltaic polymer/fullerene blend composition ratio on microstructure evolution during film solidification investigated in real time by x-ray diffraction," *Macromolecules* **44**, 3795–3800 (2011).
46. B. Schmidt-Hansberg et al., "Moving through the phase diagram: morphology formation in solution cast polymer-fullerene blend films for organic solar cells," *ACS Nano* **5**, 8579–8590 (2011).
47. U. Aygül et al., "Molecular orientation in polymer films for organic solar cells studied by NEXAFS," *J. Phys. Chem. C* **116**, 4870–4874 (2012).
48. B. A. Collins et al., "Polarized x-ray scattering reveals non-crystalline orientational ordering in organic films," *Nat. Mater.* **11**, 536–543 (2012).
49. L. A. A. Pettersson, S. Ghosh, and O. Inganäs, "Optical anisotropy in thin films of poly(3,4-ethylenedioxythiophene)-poly(4-styrenesulfonate)," *Org. Eelctron.* **3**, 143–148 (2002).
50. M. Campoy-Quiles, P. G. Etchegoin, and D. D. C. Bradley, "On the optical anisotropy of conjugated polymer thin films," *Phys. Rev. B* **72**, 045209 (2005).
51. M. C. Gurau et al., "Measuring molecular order in poly(3-alkylthiophene) thin films with polarizing spectroscopies," *Langmuir* **23**, 834–842 (2007).
52. D. Comoretto et al., "Optical constants of highly stretch-oriented poly(p-phenylene-vinylene): a joint experimental and theoretical study," *Phys. Rev. B: Condens. Matter Mater. Phys.* **62**, 10173–10184 (2000).
53. T. Erb et al., "Structural and optical properties of both pure poly(3-octylthiophene) (P3OT) and P3OT/fullerene films," *Thin Solid Films* **450**, 97–100 (2004).
54. H. Chen et al., "The role of fullerene mixing behavior in the performance of organic photovoltaics:PCBM in low-bandgap polymers," *Adv. Funct. Mater.* **24**, 140–150 (2014).

55. M. Dadmun, University of Tennessee, private communication (2012).
56. T. Kirchartz et al., "Understanding the thickness-dependent performance of organic bulk heterojunction solar cells: the influence of mobility, lifetime, and space charge," *J. Phys. Chem. Lett.* **3**, 3470–3475 (2012).
57. M. Gruber et al., "Thermodynamic efficiency limit of molecular donor-acceptor solar cells and its application to diindenoperylene/C60-based planar heterojunction devices," *Adv. Energy Mater.* **2**, 1100–1108 (2012).
58. R. Noriega et al., "A general relationship between disorder, aggregation and charge transport in conjugated polymers," *Nat. Mater.* **12**, 1038–1044 (2013).
59. A. J. Morfa et al., "Optical characterization of pristine poly(3-hexyl thiophene) films," *J. Polym. Sci., Part B: Polym. Phys.* **49**, 186–194 (2011).
60. F. C. Spano, "Modeling disorder in polymer aggregates: the optical spectroscopy of regioregular poly(3-hexylthiophene) thin films," *J. Chem. Phys.* **122**, 234701 (2005).
61. J. Clark et al., "Role of intermolecular coupling in the photophysics of disordered organic semiconductors: aggregate emission in regioregular polythiophene," *Phys. Rev. Lett.* **98**, 206406 (2007).
62. B. A. Collins et al., "Absolute measurement of domain composition and nanoscale size distribution explains performance in PTB7:$PC_{71}BM$ solar cells," *Adv. Energy Mater.* **3**, 65–74 (2013).

Biographies of the authors are not available.